that are provided maternally or expressed during early embryogenesis but are detrimental to later steps in morphogenesis. Cell shape changes, cell rearrangements, and fluid dynamics are thought to generate both extrinsic and intrinsic forces that contribute to neural tube and ventricle formation, but the underlying molecular mechanisms are poorly understood (*42*). The study of the miR-430 family and its targets therefore provides a genetic entry point to dissect the molecular basis of brain morphogenesis.

References and Notes

1. D. P. Bartel, *Cell* **116**, 281 (2004).
2. V. Ambros, *Nature* **431**, 350 (2004).
3. G. Meister, T. Tuschl, *Nature* **431**, 343 (2004).
4. A. Grishok *et al.*, *Cell* **106**, 23 (2001).
5. G. Hutvagner *et al.*, *Science* **293**, 834 (2001).
6. Y. Lee *et al.*, *Nature* **425**, 415 (2003).
7. E. Bernstein, A. A. Caudy, S. M. Hammond, G. J. Hannon, *Nature* **409**, 363 (2001).
8. B. P. Lewis, C. B. Burge, D. P. Bartel, *Cell* **120**, 15 (2005).
9. E. Berezikov *et al.*, *Cell* **120**, 21 (2005).
10. J. M. Thomson, J. Parker, C. M. Perou, S. M. Hammond, *Nat. Methods* **1**, 47 (2004).
11. J. H. Mansfield *et al.*, *Nat. Genet.* **36**, 1079 (2004).
12. H. B. Houbaviy, M. F. Murray, P. A. Sharp, *Dev. Cell* **5**, 351 (2003).
13. B. P. Lewis, I. H. Shih, M. W. Jones-Rhoades, D. P. Bartel, C. B. Burge, *Cell* **115**, 787 (2003).
14. M. Kiriakidou *et al.*, *Genes Dev.* **18**, 1165 (2004).
15. B. John *et al.*, *PLoS Biol.* **2**, e363 (2004).
16. M. N. Poy *et al.*, *Nature* **432**, 226 (2004).
17. S. Yekta, I. H. Shih, D. P. Bartel, *Science* **304**, 594 (2004).
18. C. Z. Chen, L. Li, H. F. Lodish, D. P. Bartel, *Science* **303**, 83 (2004).
19. E. Bernstein *et al.*, *Nat. Genet.* **35**, 215 (2003).
20. C. Kanellopoulou *et al.*, *Genes Dev.* **19**, 489 (2005).
21. E. Wienholds, M. J. Koudijs, F. J. van Eeden, E. Cuppen, R. H. Plasterk, *Nat. Genet.* **35**, 217 (2003).
22. B. Ciruna *et al.*, *Proc. Natl. Acad. Sci. U.S.A.* **99**, 14919 (2002).
23. L. P. Lim, M. E. Glasner, S. Yekta, C. B. Burge, D. P. Bartel, *Science* **299**, 1540 (2003).
24. W. P. Kloosterman, E. Wienholds, R. F. Ketting, R. H. Plasterk, *Nucleic Acids Res.* **32**, 6284 (2004).
25. A. J. Giraldez *et al.*, data not shown.
26. Q. Liu *et al.*, *Science* **301**, 1921 (2003).
27. N. Doi *et al.*, *Curr. Biol.* **13**, 41 (2003).
28. Y. S. Lee *et al.*, *Cell* **117**, 69 (2004).
29. J. W. Pham, J. L. Pellino, Y. S. Lee, R. W. Carthew, E. J. Sontheimer, *Cell* **117**, 83 (2004).
30. Y. Tomari *et al.*, *Cell* **116**, 831 (2004).
31. Materials and methods are available as supporting material on *Science* Online.
32. M. E. Glasner *et al.*, in preparation.
33. J. G. Doench, P. A. Sharp, *Genes Dev.* **18**, 504 (2004).
34. Y. Lee *et al.*, *EMBO J.* **23**, 4051 (2004); published online 16 September 2004 (10.1038/sj.emboj.7600385).
35. S. Baskerville, D. P. Bartel, *RNA* **11**, 241 (2005).
36. A. F. Schier, *Curr. Opin. Genet. Dev.* **11**, 393 (2001).
37. R. J. Johnston, O. Hobert, *Nature* **426**, 845 (2003).
38. D. P. Bartel, C. Z. Chen, *Nat. Rev. Genet.* **5**, 396 (2004).
39. L. P. Lim *et al.*, *Nature* **433**, 769 (2005).
40. M. A. Blasco *et al.*, *Cell* **91**, 25 (1997).
41. T. Fukagawa *et al.*, *Nat. Cell Biol.* **6**, 784 (2004).
42. L. A. Lowery, H. Sive, *Mech. Dev.* **121**, 1189 (2004).

43. We thank T. Tuschl and S. Pfeffer for help during the initial phase of the project; E. Wienholds and R. Plasterk for *Zdicer* mutants; and C. Antonio, B. Ciruna, G. Fishell, V. Greco, S. Mango, T. Schell, W. Talbot, A. Teleman, and D. Yelon for providing helpful comments on the manuscript. A.J.G. was supported by The European Molecular Biology Organization and is currently supported by The International Human Frontier Science Program Organization fellowship. S.M.H. is a General Motors Cancer Research Foundation Scholar. A.F.S. is an Irma T. Hirschl Trust Career Scientist and an Established Investigator of the American Heart Association. This work was also supported by grants from the NIH (A.F.S. and D.P.B.).

Supporting Online Material

www.sciencemag.org/cgi/content/full/1109020/DC1
Materials and Methods
Figs. S1 to S11
References

22 December 2004; accepted 25 February 2005
Published online 17 March 2005;
10.1126/science.1109020
Include this information when citing this paper.

REPORTS

The Optical Resonances in Carbon Nanotubes Arise from Excitons

Feng Wang,[1]* Gordana Dukovic,[2]* Louis E. Brus,[2] Tony F. Heinz[1]†

Optical transitions in carbon nanotubes are of central importance for nanotube characterization. They also provide insight into the nature of excited states in these one-dimensional systems. Recent work suggests that light absorption produces strongly correlated electron-hole states in the form of excitons. However, it has been difficult to rule out a simpler model in which resonances arise from the van Hove singularities associated with the one-dimensional bond structure of the nanotubes. Here, two-photon excitation spectroscopy bolsters the exciton picture. We found binding energies of ~400 millielectron volts for semiconducting single-walled nanotubes with 0.8-nanometer diameters. The results demonstrate the dominant role of many-body interactions in the excited-state properties of one-dimensional systems.

Coulomb interactions are markedly enhanced in one-dimensional (1D) systems. Single-walled carbon nanotubes (SWNTs) provide an ideal model system for studying these effects. Strong electron-electron interactions are associated with many phenomena in the charge transport of SWNTs, including Coulomb blockade (*1*, *2*), Kondo effects (*3*, *4*), and Luttinger liquid behavior (*5*, *6*). The effect of Coulomb interactions on nanotube optical properties has remained unclear, in spite of its central importance both for a fundamental understanding of these model 1D systems (*7*–*9*) and for applications (*7*, *10*, *11*). Theoretical studies suggest that optically produced electron-hole pairs should, under their mutual Coulomb interaction, form strongly correlated entities known as excitons (*12*–*18*). Although some evidence of excitons has emerged from studies of nanotube optical spectra (*7*, *19*) and excited-state dynamics (*20*), it is difficult to rule out an alternative and widely used picture that attributes the optical resonances to van Hove singularities in the 1D density of states (*21*–*23*). Here, we demonstrate experimentally that the optically excited states of SWNTs are excitonic in nature. We measured exciton binding energies that represent a large fraction of the semiconducting SWNT band gap. As such, excitonic interactions are not a minor perturbation as in comparable bulk semiconductors, but actually define the optical properties of SWNTs. The importance of many-body effects in nanotubes derives from their 1D character; similar excitonic behavior is also seen in organic polymers with 1D conjugated backbones (*24*).

We identified excitons in carbon nanotubes using two-photon excitation spectroscopy. Two-photon transitions obey selection rules distinct from those governing linear excitation processes and thereby provide complementary insights into the electronic structure of excited states, as has been demonstrated in studies of molecular systems (*25*) and bulk solids (*26*). In 1D materials like SWNTs, the exciton states show defined symmetry with respect to reflection through a plane perpendicular to the nanotube axis. A Rydberg series of exciton states describing the relative motion of the electron and hole, analogous to the hydrogenic states, is then formed with definite parity with respect to this reflection plane. The even states are denoted as 1*s*, 2*s*, 3*s*, and so on, and the odd wave functions are labeled as 2*p*, 3*p*, and so on (*27*). Because of the weak spin-

[1]Departments of Physics and Electrical Engineering, [2]Department of Chemistry, Columbia University, 538 West 120th Street, New York, NY 10027, USA.

*These authors contributed equally to this work.
†To whom correspondence should be addressed. E-mail: tony.heinz@columbia.edu

orbit coupling in SWNTs, all optically active excitons are singlet states, with the allowed transitions being governed by electric-dipole selection rules. For the dominant transitions polarized along the nanotube axis, one-photon (linear) excitation requires the final and initial states to exhibit opposite symmetry. In contrast, a two-photon transition is allowed only when the final state has the same parity as the initial state. Given the symmetry of the underlying atomic-scale wave functions, one-photon excitation produces only excitons of *s*-symmetry, whereas two-photon excitation leads only to excitons of *p*-symmetry (*28*). Thus, one-photon transitions access the lowest lying 1*s* exciton; two-photon transitions access only the excited states of the exciton.

An experimental method to determine the energies of the ground and excited exciton states follows immediately from these symmetry arguments: We measured the energies needed for one-photon and two-photon transitions in semiconducting nanotubes (Fig. 1A). A comparison of these energies yields the energy difference between the ground and excited exciton states and thereby directly indicates the exciton binding strength. When the excitonic interactions were negligible, we reverted to a simple band picture in which the onset of two-photon absorption coincides with the energy of one-photon absorption (Fig. 1B). The two-photon excitation spectra reflect the qualitative difference between these two pictures in an unambiguous fashion. In contrast, conventional linear optical measurements, such as absorption and fluorescence spectroscopy, access only one-photon transitions, for which a van Hove singularity and a broadened excitonic resonance exhibit qualitatively similar features. Because the one-photon absorption and emission arise from the same electronic transition in SWNTs, there is no Stokes shift between the two, as apparent in comparison of absorption and fluorescence spectra (*8*).

In our experiment, we used isolated SWNTs in a poly(maleic acid/octyl vinyl ether) (PMAOVE) matrix. SWNTs grown by high-pressure CO synthesis were dispersed in an aqueous solution of PMAOVE by a sonication method (*29*). In order to minimize infrared absorption of water, we formed a film of SWNTs imbedded in polymer matrix by slowly drying a drop of the solution. The SWNT samples obtained by this procedure showed fluorescence emission comparable to that of the SWNTs in aqueous solution.

Two-photon excitation is a nonlinear optical effect that requires the simultaneous absorption of a pair of photons. Femtosecond laser pulses provided the high intensities of light necessary to drive this process. The light source, a commercial optical parametrical amplifier (Spectra Physics OPA-800C), pumped by an amplified mode-locked Ti:sapphire laser, produced infrared pulses of 130-fs duration at a 1-kHz repetition rate. Peak powers exceeding 10^8 W were obtained over a photon energy range from 0.6 to 1.0 eV. Because these photon energies were well below the 1-photon absorption threshold (>1.2 eV) of the relevant SWNTs, no linear excitation occurred. A laser fluence of 5 J/m^2 was typically chosen for the measurements. At this fluence, we explicitly verified the expected quadratic dependence of the excitation process on laser intensity.

To detect the two-photon excitation process in the SWNTs, we did not directly measure the depletion of the pump beam. Rather, we used the more sensitive approach of monitoring the induced light emission. The scheme can thus be described as two-photon–induced fluorescence excitation spectroscopy. Prior studies have shown that rapid excited-state relaxation processes in SWNTs (*20*) lead to fluorescence emission exclusively from the 1*s*-exciton state. Measurement of the two-photon–induced fluorescence thus yielded (Fig. 1A) both two-photon absorption spectra (from the fluorescence strength as a function of the laser excitation wavelength) and the one-photon 1*s*-exciton spectra (from the fluorescence emission wavelength). Further, because the fluorescence peaks reflect the physical structure of the emitting nanotubes, we obtained structure-specific excitation spectroscopy even when probing an ensemble sample. We detected the fluorescence emission in a backscattering geometry, using a spectrometer with 8-nm spectral resolution and a 2D array charge-coupled device (CCD) detector. Our data sampled the infrared excitation range in 10-meV steps.

The measured two-photon excitation spectra (Fig. 2) show the strength of fluorescence emission as a function of both the (two-photon) excitation energy and the (one-photon) emission energy. From the 2D contour plot, distinct fluorescence emission features emerge at emission energies of 1.21, 1.26, 1.30, and 1.36 eV (Fig. 2, circles). These emission peaks have been assigned, respectively, to SWNTs with chiral indices of (7,5), (6,5), (8,3), and (9,1) (*7*). It is apparent that none of the nanotubes were excited when the two-photon excitation energy was the same as the emission energy (Fig. 2, solid line). Only when the excitation energy was substantially greater than the emission energy did two-photon absorption occur. This behavior is a signature of the presence of excitons with significant binding energy and is incompatible with a simple band picture of the optical transitions.

The two-photon excitation spectra for nanotubes of given chiral index can be obtained as a horizontal cut in the contour plot of Fig. 2, taken at an energy corresponding to 1*s*-exciton emission of the relevant SWNT. To enhance the quality of the data, we applied a fitting procedure (*30*) to eliminate background contributions from the emission of other nanotube species. The resulting two-photon excitation spectra are shown for the (7,5), (6,5), and (8,3) SWNTs in Fig. 3. For each of the SWNT structures, the energy of the 1*s* fluorescence emission is indicated by an arrow.

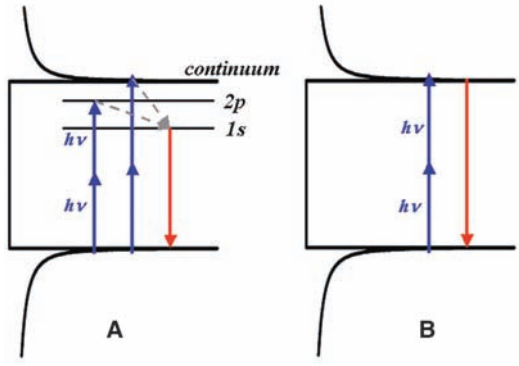

Fig. 1. Schematic representation of the density of states for a SWNT, showing the two-photon excitation (blue arrows) with photon energy *h*ν and subsequent fluorescence emission (red arrows) in the exciton and band pictures. (**A**) In the exciton picture, the 1*s* exciton state is forbidden under two-photon excitation. The 2*p* exciton and continuum states are excited. They relax to the 1*s* exciton state and fluoresce through a one-photon process. (**B**) In the band picture, the threshold for two-photon excitation lies at the band edge, where the relaxed fluorescence emission also takes place.

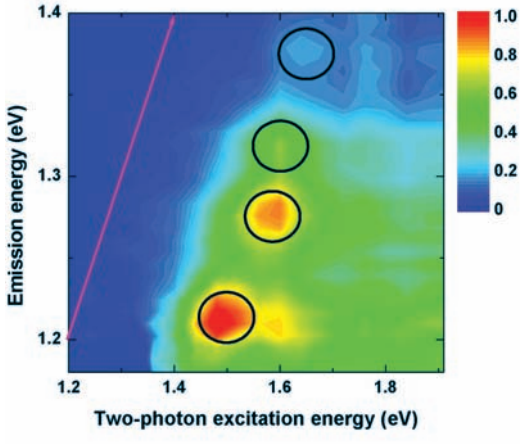

Fig. 2. Contour plot of two-photon excitation spectra of SWNTs. The measured fluorescence intensity is shown in a false-color representation as a function of the (two-photon) excitation energy and the (one-photon) fluorescence emission energy. Fluorescence peaks of different SWNT species [(7,5), (6,5), (8,3), and (9,1) with increasing emission energy] can be identified (black circles). The two-photon excitation peaks are shifted substantially above the energy of the corresponding emission feature, as is apparent by comparison with the solid line describing equal excitation and emission energies. The large shift arises from the excitonic nature of SWNT optical transitions.

The peaks in the two-photon excitation spectra can be assigned to the energy for creation of the $2p$ exciton, the lowest lying symmetry-allowed state for the nonlinear excitation process. From a comparison of this energy with that of the $1s$-exciton emission feature, we obtained directly the relevant energy differences for the ground and excited exciton states: $E_{2p} - E_{1s}$ = 280, 310, and 300 meV, respectively, for the (7,5), (6,5), and (8,3) SWNTs.

To determine the exciton binding energy and understand the nature of the two-photon spectra more fully, we considered the two-photon excitation process in greater detail. In addition to two-photon transitions to the $2p$ state, higher lying bound excitons are also accessible (such as $3p$ and $4p$). The strength of these transitions was relatively small, and they do not account for the main features of the spectrum. We also, however, have transitions to the continuum or unbound exciton states. Including the influence of electron-hole interactions on the continuum transitions, we found that the expected shape of this contribution to the two-photon excitation spectrum could be approximated by a step function near the band edge (*31*). The experimental two-photon excitation spectra can be fit quite satisfactorily to the sum of a Lorentzian $2p$ exciton resonance and the continuum transitions with a broadened onset.

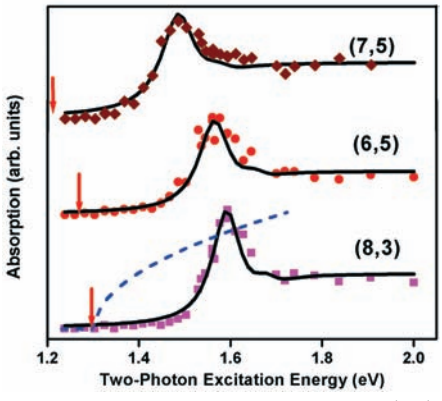

Fig. 3. Two-photon excitation spectra of (7,5), (6,5), and (8,3) SWNTs. The traces, offset for clarity, show onset energies for two-photon transitions that are appreciably higher than the corresponding fluorescence peaks (indicated by the arrows). The solid lines are the fits to the excitation spectrum obtained from our exciton model. For comparison, we show the single-particle band model prediction for an (8,3) nanotube as the dashed line in the lower trace.

A more quantitative description of the two-photon excitation spectra can be achieved with a specific model of the effective electron-hole interaction within a SWNT. In the model, we consider a truncated 1D Coulomb interaction given by the potential $V(z) = -e^2/[\varepsilon(|z| + z_0)]$ for electron-hole separation z. The value of $z_0 = 0.30d$ is fixed to approximate the Coulomb interaction between two charges distributed as rings at a separation z on a cylindrical surface of diameter d (*27*); the effective dielectric screening ε is the only adjustable parameter in the analysis. This simple model provides a good fit to the experimental data for the different nanotube species examined when we use an effective dielectric constant of 2.5 (Fig. 3, solid line). The features predicted in the model have been broadened by 80 meV (full width at half maximum). This broadening is in part experimental, reflecting the spectral width of the short laser excitation pulses (30 meV). The main contribution, however, is the width of the excitonic transition itself. This width is ascribed to lifetime broadening associated with the rapid relaxation of the excited states to the $1s$ exciton state (*20*). From this analysis, we determined the energy of $2p$ for the three SWNT species in Fig. 3 to be $E_{2p} \approx -120$ meV with respect to the onset of the continuum states at the band gap energy E_g.

Combining the previously determined $E_{2p} - E_{1s}$ energy difference with the position of the $2p$ exciton relative to the continuum, we obtained an overall binding energy for the ground-state ($1s$) exciton of $E_{ex} = (E_g - E_{1s}) \approx$ 420 meV for the investigated SWNTs. This value is comparable to recent theoretical predictions of large exciton binding energies (*13*, *14*). The exciton binding energy thus constitutes a substantial fraction of the gap energy $E_g \approx 1.3$ eV for our 0.8-nm SWNTs. To put this result in context, the exciton binding energies in bulk semiconductors typically lie in the range of several meV and represent a slight correction to the band gap. Furthermore, because thermal energies at room temperature exceed typical bulk exciton binding energies, excitonic effects in bulk materials can be largely neglected under ambient conditions. This situation clearly does not prevail for SWNTs.

We can understand the strong increase in excitonic effects in the SWNTs as the consequence of two factors. The first arises from a general property of reduced dimensionality: In three dimensions, the probability of having an electron and hole separated by a displacement of r includes a phase space factor of r^2, favoring larger separations over smaller ones. In one dimension, no such factor exists. Short separations are thus of greater relative importance, and the role of the Coulomb interactions is enhanced. The second factor relates to the decreased dielectric screening for a quasi-1D SWNT system. This effect arises because the electric field lines generated by the separated electron-hole pair travel largely outside of the nanotube, where dielectric screening is decreased. Because these effects are general features arsing from the 1D character, they should be widely present in 1D systems. Indeed, similar excitonic effects have been extensively studied in a large family of 1D structures of conjugated polymers (*24*).

To help visualize the strongly bound excitons in SWNTs, we estimated the exciton's spatial extent, i.e., the typical separation between the electron and the hole in the correlated exciton state. Assuming an exciton kinetic energy comparable to its binding energy E_{ex}, which applies precisely for 3D excitons, we obtain the relation $E_{ex} \sim \hbar^2/2mR^2$, where $\hbar$ is Planck's constant h divided by 2π, m is the reduced electron-hole mass, and R is the exciton radius. For $m = 0.05\ m_0$ (*21*), we deduced from our experimental binding energy a ground-state exciton radius of $R = 1.2$ nm. This value is similar to that obtained by calculation within the truncated Coulomb model specified above. Figure 4 provides a representation of the calculated density distribution of the exciton envelope wave function. The result is a highly localized entity, with a spatial extent along the nanotube axis only slightly exceeding the nanotube radius of 0.8 nm.

The importance of excitonic effects is clear for the interpretation and assignment of the observed optical spectra, as discussed in the literature on the relation of the E_{11} and E_{22} transition energies in SWNTs (*7*, *15*, *17*). The excitonic character of the optically excited state also has immediate implications for optoelectronic devices and phenomena. For example, photoconductivity in SWNTs should have a strong dependence on the applied electric field, because charge transport requires spatial separation of the electron-hole pair. The excitonic character of optically excited SWNTs also raises the possibility of modifying the SWNT transitions through external perturbations, thus facilitating new electro-optical modulators and sensors. More broadly, the strong electron-hole interaction demonstrated in our study highlights the central role of many-body effects in 1D materials.

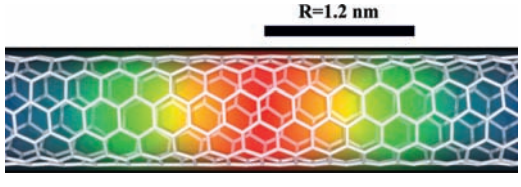

Fig. 4. Density of the $1s$-exciton envelope wave function for a (6,5) SWNT. The wave function has been calculated using the experimentally determined exciton binding energy and the truncated Coulomb electron-hole interaction. The density represents the probability of finding the electron and hole composing the exciton at the indicated relative separation. The half width of the exciton along the nanotube is $R = 1.2$ nm, compared to the 0.8-nm diameter of the nanotube.

References and Notes

1. M. Bockrath *et al.*, *Science* **275**, 1922 (1997).
2. S. J. Tans *et al.*, *Nature* **386**, 474 (1997).
3. T. W. Odom, J. L. Huang, C. L. Cheung, C. M. Lieber, *Science* **290**, 1549 (2000).
4. J. Nygard, D. H. Cobden, P. E. Lindelof, *Nature* **408**, 342 (2000).
5. M. Bockrath *et al.*, *Nature* **397**, 598 (1999).

6. H. Ishii *et al.*, *Nature* **426**, 540 (2003).
7. S. M. Bachilo *et al.*, *Science* **298**, 2361 (2002).
8. M. J. O'Connell *et al.*, *Science* **297**, 593 (2002).
9. M. Y. Sfeir *et al.*, *Science* **306**, 1540 (2004).
10. J. A. Misewich *et al.*, *Science* **300**, 783 (2003).
11. M. Freitag, Y. Martin, J. A. Misewich, R. Martel, Ph. Avouris, *Nano Lett.* **3**, 1067 (2003).
12. T. Ando, *J. Phys. Soc. Jpn.* **66**, 1066 (1997).
13. T. G. Pedersen, *Phys. Rev. B* **67**, art. no. 073401 (2003).
14. V. Perebeinos, J. Tersoff, Ph. Avouris, *Phys. Rev. Lett.* **92**, art. no. 257402 (2004).
15. C. D. Spataru, S. Ismail-Beigi, L. X. Benedict, S. G. Louie, *Phys. Rev. Lett.* **92**, art. no. 077402 (2004).
16. E. Chang, G. Bussi, A. Ruini, E. Molinari, *Phys. Rev. Lett.* **92**, art. no. 196401 (2004).
17. C. L. Kane, E. J. Mele, *Phys. Rev. Lett.* **90**, art. no. 207401 (2003).
18. H. B. Zhao, S. Mazumdar, *Phys. Rev. Lett.* **93**, art. no. 157402 (2004).
19. H. Htoon, M. J. O'Connell, P. J. Cox, S. K. Doorn, V. I. Klimov, *Phys. Rev. Lett.* **93**, art. no. 027401 (2004).
20. Y. Z. Ma *et al.*, *J. Chem. Phys.* **120**, 3368 (2004).
21. R. Saito, G. Dresselhaus, M. S. Dresselhaus, *Physical Properties of Carbon Nanotubes* (Imperial College Press, London, 1998).
22. A. Hagen, T. Hertel, *Nano Lett.* **3**, 383 (2003).
23. M. S. Dresselhaus, G. Dresselhaus, A. Jorio, *Annu. Rev. Mater. Res.* **34**, 247 (2004).
24. R. Farchioni, G. Grosso, Eds., *Organic Electronic Materials: Conjugated Polymers and Low Molecular Weight Organic Solids* (Springer, Berlin, 2001).
25. P. R. Callis, *Annu. Rev. Phys. Chem.* **48**, 271 (1997).
26. Y. R. Shen, *The Principles of Nonlinear Optics* (Wiley, New York, 1984).
27. T. Ogawa, T. Takagahara, *Phys. Rev. B* **44**, 8138 (1991).
28. A. Shimizu, T. Ogawa, H. Sakaki, *Phys. Rev. B* **45**, 11338 (1992).
29. G. Dukovic *et al.*, *J. Am. Chem. Soc.* **126**, 15269 (2004).
30. To eliminate the influence of background in determining the two-photon excitation spectrum of SWNTs of a given chiral index, we plotted the experimental emission spectra, corresponding to vertical cuts in the two-dimension contour plot of Fig. 2, for a series of two-photon excitation energies. We then fit each emission spectrum to a sum of Lorentzian features corresponding to the relevant nanotube species in our ensemble sample. The two-photon excitation spectrum for a given nanotube chiral index was then obtained by tracking the peak height of corresponding fluorescence contribution as a function of the two-photon excitation energy.
31. For the continuum states in a 1D direct-gap material, the two-photon absorption cross section σ_{TPA} scales as $\sigma_{TPA} \propto (E - E_g)^{1/2}$ within the free carrier picture, where E denotes the photon energy and E_g the bandgap energy. This form is modified by strong electron-hole interactions. Within the Wentzel-Kramers-Brillouin approximation, one can show generally that this correction leads to an enhancement near the band edge that produces a step function for the two-photon cross-section, $\sigma_{TPA} \propto \theta(E - E_g)$, where θ is the usual Heavyside function. This correction is analogous to the well-known result for one-photon excitonic transitions in bulk semiconductors (*32*).
32. R. J. Elliott, *Phys. Rev.* **108**, 1384 (1957).

33. We would like to thank Ph. Avouris, M. Hybertsen, M. Loy, P. Kim, V. Perebeinos, and M. Sfeir for helpful discussions. Supported by the Nanoscale Science and Engineering Initiative of the NSF (grant no. CHE-0117752), by the New York State Office of Science, Technology, and Academic Research, and by the U.S. Department of Energy Office of Basic Energy Sciences (grant nos. DOE-FG02-98ER14861 and DE-FG02-03ER15463).

26 January 2005; accepted 14 March 2005
10.1126/science.1110265

Zircon Thermometer Reveals Minimum Melting Conditions on Earliest Earth

E. B. Watson[1]* and T. M. Harrison[2,3]

Ancient zircons from Western Australia's Jack Hills preserve a record of conditions that prevailed on Earth not long after its formation. Widely considered to have been a uniquely violent period geodynamically, the Hadean Eon [4.5 to 4.0 billion years ago (Ga)] has recently been interpreted by some as far more benign—possibly even characterized by oceans like those of the present day. Knowledge of the crystallization temperatures of the Hadean zircons is key to this debate. A thermometer based on titanium content revealed that these zircons cluster strongly at ~700°C, which is indistinguishable from temperatures of granitoid zircon growth today and strongly suggests a regulated mechanism producing zircon-bearing rocks during the Hadean. The temperatures substantiate the existence of wet, minimum-melting conditions within 200 million years of solar system formation. They further suggest that Earth had settled into a pattern of crust formation, erosion, and sediment recycling as early as 4.35 Ga.

The first 500 million years of Earth evolution, a period known as the Hadean Eon, was the most geodynamically vigorous in our planet's history. During this time, it is variously speculated that the Earth may have experienced collision with a Mars-sized object (*1*), formed a global magma ocean (*2*), grown the first continents (*3*), and seen the emergence of life (*4*). It is also entirely possible, and consistent with the geochemical record, that none of these events took place. The fundamental problem is that we have no rock record from this interval to learn about these processes because the oldest firmly dated rock is 4.04 Ga (*5*). How, then, are we to gain further insights into the formative stages of Earth evolution?

Although no Hadean rocks are yet documented, we are not entirely without a geochemical record of the period between 4.5 and 4.0 Ga. The existence of zircons >4.1 Ga preserved in Early Archean metasediments at Mt. Narryer and Jack Hills, Western Australia, has been known for more than 20 years (*6*, *7*), and recent measurements have begun to glean information from them regarding the nature of the Hadean Earth. For example, Hf isotopic studies suggest the existence of reworked continental crust before 4.1 Ga (*8*). Oxygen isotope results have been interpreted as indicating that protoliths of ~4.3-Ga magmas formed in the presence of water at the Earth's surface (*9*, *10*). Xenon isotopic studies of these ancient zircons have permitted an estimate of the initial terrestrial plutonium/uranium ratio, a parameter key to understanding the origin and evolution of the atmosphere (*11*).

These and other results have challenged the traditional view that continental formation and development of a hydrosphere were frustrated by meteorite bombardment and basaltic igneous activity until ~4 Ga. Instead, they suggest a surface environment and petrogenetic processes much more similar to those of the present day. Here, we exploit a newly developed thermometer, based on Ti incorporation into crystallizing zircon, to assess the nature of Hadean magmatism. From these analyses, we conclude that Jack Hills zircons were dominantly sourced from crustal melts that formed at temperatures ranging from those characteristic of wet, minimum melting to vapor absent melting under anatectic conditions.

Titanium content is uniquely suitable as a potential indicator of zircon crystallization temperature. As a tetravalent ion under all relevant geologic conditions, Ti enters the zircon lattice in homovalent replacement of Zr^{4+} or Si^{4+}. Consequently, Ti uptake does not depend on the availability of other charge-compensating ions. For the TiO_2-saturated case (i.e., rutile present in the system), the thermodynamic basis of the thermometer is the simple reaction

$$TiO_{2(\text{rutile})} = TiO_{2(\text{zircon})} \qquad (1)$$

for which the equilibrium constant is

$$k_1 = \frac{a_{TiO_2}^{\text{zircon}}}{a_{TiO_2}^{\text{rutile}}}$$

where a_{TiO_2} is the activity of TiO_2 in rutile or zircon as indicated by the superscript. Because rutile is nearly pure TiO_2, $a_{TiO_2}^{\text{rutile}} \sim 1$, so

[1]Department of Earth and Environmental Sciences, Rensselaer Polytechnic Institute, Troy, NY 12180, USA. [2]Research School of Earth Sciences, Australian National University, Canberra, ACT 2601, Australia. [3]Department of Earth and Space Sciences and Institute of Geophysics and Planetary Physics, University of California, Los Angeles, CA 90095, USA.

*To whom correspondence should be addressed. E-mail: watsoe@rpi.edu